Optical Imaging of Immune Response Following Synergistic Immune Photothermal Therapy (SYMPHONY) for Bladder Cancer Using A Murine Window Chamber Model

by

Yuxiang Wang

Medical Physics Program
Duke Kunshan University and Duke University

Date: _____

Approved:

_____
Gregory Palmer, Advisor

_____
Mark Dewhirst

_____
Xin Chen

A thesis submitted in partial fulfillment of
the requirements for the degree of
Master of Science in Medical Physics of
the Medical Physics Program in the Graduate School of
Duke Kunshan University and Duke University

2020

ABSTRACT

Optical Imaging of Immune Response Following Synergistic Immune Photothermal Therapy (SYMPHONY) for Bladder Cancer Using A Murine Window Chamber Model

by

Yuxiang Wang

Medical Physics Program
Duke Kunshan University and Duke University

Date: _____

Approved:

_____
Gregory Palmer, Advisor

_____
Mark Dewhirst

_____
Xin Chen

An abstract of a thesis submitted in partial
fulfillment of the requirements for the degree of
Master of Science in Medical Physics of
the Medical Physics Program in the Graduate School of
Duke Kunshan University and Duke University

2020

Abstract

An abstract of a thesis: Cancer is a significant threat to human health with more than eight million deaths each year in the world. Therefore, numerous technologies have been implemented or under development to effectively treat cancer.

One novel therapeutic platform is implemented using nanoparticle-mediated photothermal therapy. Gold NanoStars (GNS), are a unique form of gold nanoparticles (GNPs) that have unique therapeutic potential because of their star-shaped geometry. Enhanced light absorption and higher photon-to-heat conversion efficiency are introduced by GNS's plasmonic properties. In the application of hyperthermia, this photothermal process can be exploited to specifically heat tumors and, more importantly, to amplify the antitumor immune response following the highly immunogenic thermal death of cancer cells. Meanwhile, when combined with immune checkpoint inhibition immunotherapy (IT), this SYnergistic iMmuno PHOtothermal NanotherapY (SYMPHONY) has been shown to reverse tumor-mediated immunosuppression, thereby leading to the treatment of not only primary tumors but also cancer metastasis. This phenomenon is called the "abscopal effect". However, the immune response has not been clearly quantified yet. Our hypothesis was that different treatment modalities (PTT only, GNS-PTT, IT, SYMPHONY) will trigger different levels

of immune response including the decrease of immunosuppressive cells and the influx of cytotoxic cells, which could be observed by imaging immune cell reporters.

Accordingly, two specific aims were set for this study: 1. to develop a pre-clinical murine model to quantify different levels of immune response mimicking the tumor metastatic environment; 2. to quantify immune response following SYMPHONY using imaging analysis techniques.

To achieve the specific aims, window chamber models combined with in vivo fluorescence imaging techniques provide an ideal platform to mimic cancer metastasis in the chamber and longitudinally monitor immune response through the prevalence of fluorescent reporters specifically localized to immune cells of interest. We utilized a dual tumor mouse model, consisting of a primary tumor grown in the flank of the mouse which received the SYMPHONY therapy, as well as a secondary tumor located in the window chamber through which we could image and observe the abscopal response to therapy. In this study, we demonstrate the optical imaging procedure following synergistic immune photothermal therapy (SYMPHONY) of bladder cancer using the immune-GFP-labeled murine window chamber model, for the purpose of quantifying the immune response at this mimicked-tumor metastasis site. Four groups were established: the SYMPHONY group, the photothermal therapy group, the immune therapy group, and the Gold NanoStars (GNS) control group.

Higher immune responses were observed in the tumor regions compared to the non-tumor regions. The in vivo fluorescence imaging along with the window chamber technique demonstrates the feasibility and convenience of following such a longitudinal study like SYMPHONY. However, although temporal changes in reporter intensity were observed, with a limited number of samples, we cannot thus far identify significant differences among the treatment groups. Approaches for further characterizing this model are discussed.

Contents

List of Tables

List of Figures

Acknowledgements

I would like to express my most sincere thankfulness to my advisor and mentor, Dr. Gregory Palmer in the Department Radiation Oncology at Duke University, for his constructive suggestion and advice for this research project, and also the patient guidance and incentive encouragement for my graduate study. He was always available when I encountered confusion in knowledge or trouble in experiments. He was always there smiling, explaining, and mentoring, both academically and mentally.

I am grateful to all the lovely members of the Palmer Lab: thanks to M.D. Antoine Mansourati who gave me hand-on guidance on animal experiments; thanks to PhD candidate Ashlyn Rickcard for her advice on imaging processing and analysis, and sharing of a PhD life; thanks to Kenneth Young for his guidance on experimental safety and assistance in the use of laboratory apparatus; thanks to Keith Laemont for his advice on career choice and professionalism.

Additionally, I would like to acknowledge my committee members: Dr. Gregory Palmer, Dr. Mark Dewhirst and Dr. Xin Chen. Their time and support are appreciated.

A special gratitude to Dr. James Bowsher, a faculty member of the Medical Physics Graduate Program, I appreciate his support and advice. His words will continue to guide me in the future.

To the Medical Physics faculty, staff and students: thank you for your help and support. I have learned a great deal from everyone in this program.

Lastly, I would like to thank my family and friends. Their priceless encouragement and support through my growth help me to overcome difficulties one after another. Thank you!

1. Introduction

1.1 Bladder Cancer (BC)

Bladder cancer (BC) is the 4th most common cancer in men and the 11th most common in women [10]. At diagnosis, ~80% of BCs are early-stage non-muscle invasive bladder cancer (NMIBC) for which the 5-year survival is excellent. However, the majority of NMIBC patients will experience a cancer recurrence. This requires repeated surgery and/or other treatments, like bacillus Calmette-Guérin (BCG) immunotherapy, to avoid cancer progression to a life-threatening state. Radical removal of the bladder (cystectomy) is the primary treatment for more invasive BC, but half of the patients with muscle-invasive BC will die despite treatment [13]. BC also has the highest lifetime per-patient cost of all cancers, because of its high recurrence rate [11-12]. Additionally, the patient's quality of life is severely affected by regular bladder surveillance with cystoscopy and the subsequent treatment of recurrence. Their quality of life is also influenced by a reduced bladder capacity. As the capacity is reduced, the frequency of urination episodes goes up. Therefore, there is a significant clinical need for novel and effective approaches to managing bladder cancer.

1.2 PD-L1/PD-1 Immune Checkpoint Inhibition as A Method of Bladder Cancer Immunotherapy in Bladder Cancer

Immunotherapy has long been a critical part of the BC treatment. For instance, bacillus Calmette-Guérin (BCG) [14], reduces the incidence of recurrent NMIBC while reducing the risk of progression to MIBC [15]. However, BCG is ineffective in MIBC. Therefore, systematic immunotherapies are under development for MIBC or more advanced BC.

Inman et al. reported that a T cell co-stimulation molecule called programmed death ligand 1 (PD-L1) was associated with BCG immunotherapy failure and worsening BC stage [16]. The PD-L1 immune checkpoint is commonly expressed by many cancers as a method of immune evasion [17, 18]. PD-L1 binds to the PD-1 receptor; this interaction inhibits T-cell function, thus allowing cancer to escape the immune response. It was found that the PD-L1 blockade was a therapeutic possibility for cancer. To reverse tumor-mediated immunosuppression, antibodies blocking the PD-1/PD-L1 interaction have been utilized. However, immunotherapy alone is not curative in BC so far.

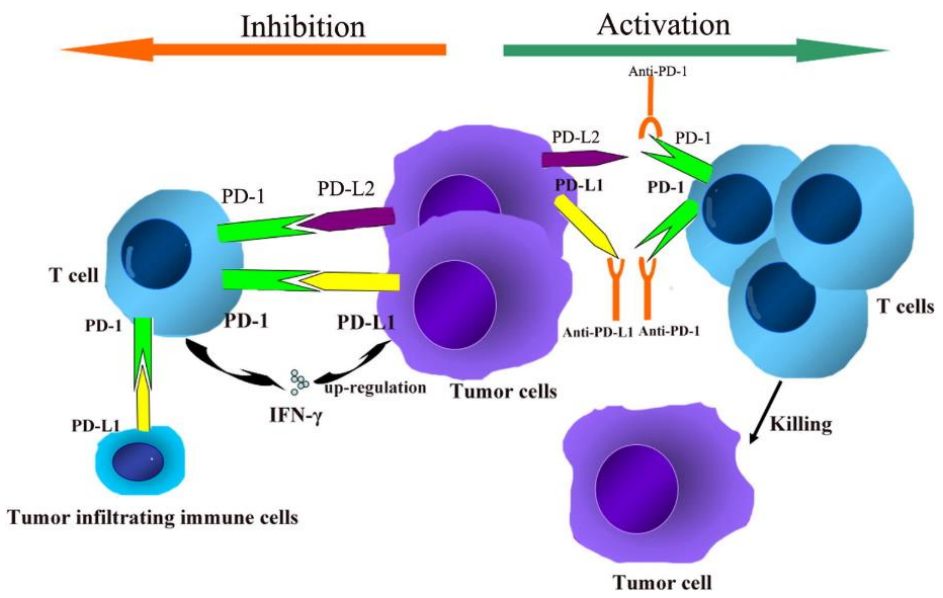

Figure 1: Schematic illustration of the mechanism of the PD-L1/PD-1 Immune Checkpoint Inhibition/Activation [33].

1.3 Plasmonic Gold NanoStars (GNS)–Mediated Photothermal Therapy (PTT)

Hyperthermia (HT) is a treatment where heat is applied to a tumor or organ [2]. Different temperature ranges of hyperthermia have various effects. High-temperature HT (> 55°C) can induce immediate death (thermal ablation) in a tumor; mild fever -range HT (40-43°C) has an influence in (1) improving cancer cell sensitivity to anti-cancer therapy, (2) improving drug delivery to tumors, and (3) triggering potent systemic anti-cancer immune responses [3-5]. In a way, HT is actually a combination of HT and immunotherapy.

When a tumor is heated, an important vascular physiological effect called vasodilation occurs, which increases blood flow to the tumor and adjacent tissue. On the

cellular level, heat also makes the cellular lipid-protein bilayer more permeable [3]. These two factors make an already leaky tumor vasculature even leakier. The phenomena by which tumor vessels exhibit leakiness in general is known as, the enhanced permeability and retention (EPR) effect [6].

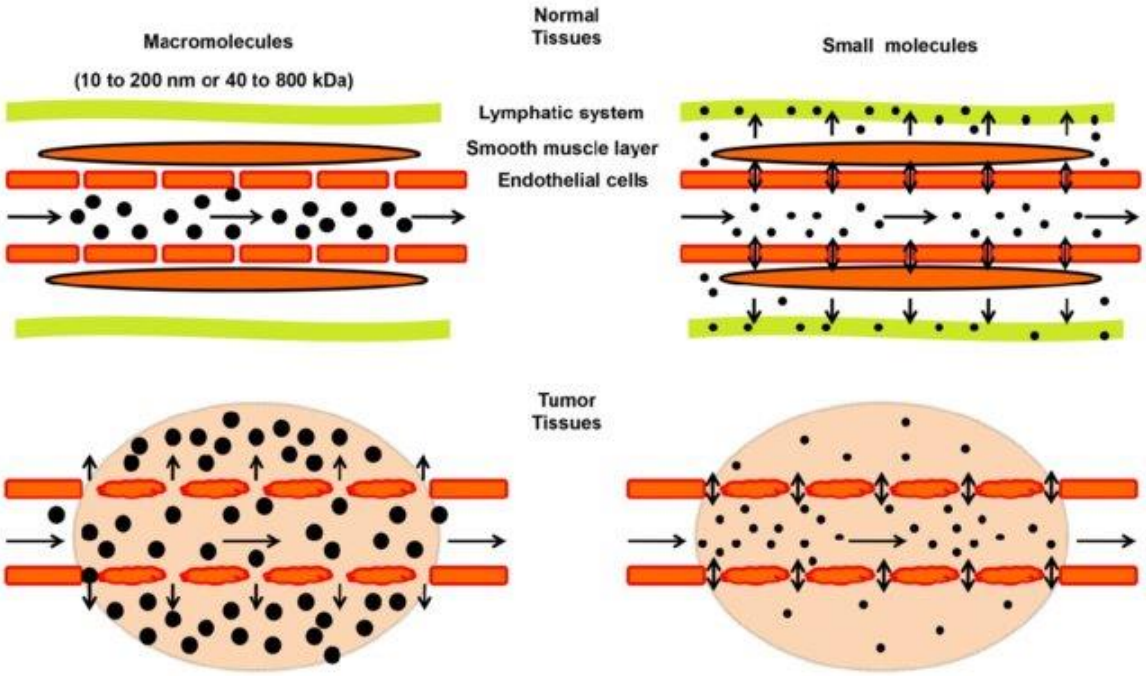

Figure 2: Schematic illustration of the enhanced permeability and retention (EPR) effect in tumors. In tumor tissues (lower panels), endothelial cells are poorly aligned with wide fenestrations compared to normal tissues (top panels). Therefore, macromolecules (10 to 200 nm or 40 to 800 kDa) tend to accumulate in tumor tissues much more than in normal tissues. In contrast, small molecules diffuse freely in and out of blood vessels in both normal and tumor tissues due to their small sizes, leading to their low concentrations over time [34].

In Nanoparticle (NP)-mediated thermal therapy, Nanoparticles are targeted to the tumor sites with the contribution of the EPR effect, followed by irradiation with an

external energy source like a laser to produce heat [9]. Due to efficient photon absorption and photon-to-heat conversion provided by the nanoparticles, the tumor accumulated with GNS gets a higher thermal dose while normal tissue is spared and maintained at a lower temperature.

Among nanoparticles used for photothermal therapy (PTT), Gold Nanostars (GNS) are of particular interest for the following reasons: (1) Engineering subtle changes in their geometry offers a wide range of optical tunability. The multiple sharp branch tips on GNS create a "lightning rod" effect of local electromagnetic field enhancement, enhancing local photon conversion to heat [7]. (2) GNS preferentially accumulate in tumors [8]. GNS-mediated PTT shows better treatment outcomes than traditional PTT as a selective cancer therapy at the nanoscale [8].

To summarize this introductory session, plasmonic Gold NanoStars (GNS)–mediated photothermal therapy (PTT) provides another approach to managing bladder cancer.

1.4 SYMPHONY

SYMPHONY therapy is named as SYnergistic iMmuno PHOtothermal NanotherapY. It combines PD-L1/PD-1 immune checkpoint inhibition with GNS-mediated PTT for a two-pronged treatment modality to address both primary and metastatic cancers.

To be specific, first, tumor-localized PTT with GNS and NIR irradiation kills the primary tumor cells. Second, dying tumor cells release tumor-specific antigens and damage-associated molecular patterns (DAMPs), including heat shock proteins (HSPs) into the tumor microenvironment [19]. Third, DAMPs actively stimulate the immune response by modulating maturation, activation, and presentation of antigen-presenting cells (APCs). Lastly, these activated APCs present tumor antigens to T cells, activating adaptive immunity. Blocking PD-L1/PD-1 signaling using antibodies during T cell activation amplifies total immune response.

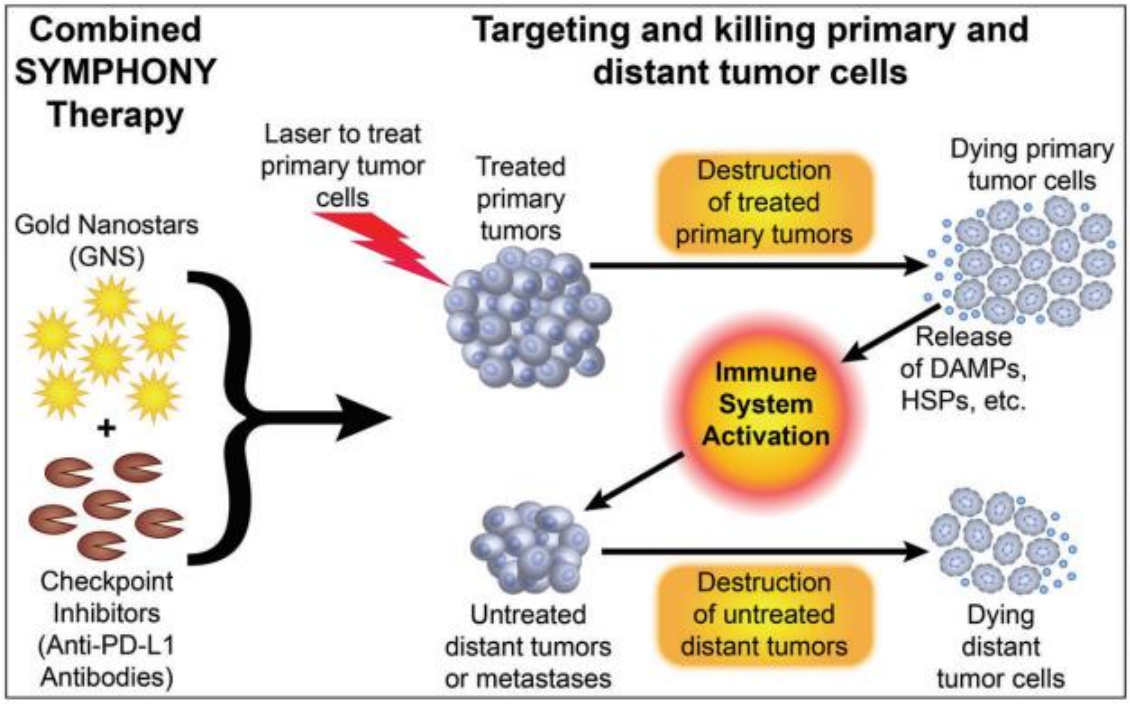

Figure 3: Schematic illustration of the synergistic immuno photothermal nanotherapy (SYMPHONY).

One preliminary study collaborated by Yang, Maccarini, Palmer et al. [35] from Duke University showed that SYMPHONY achieved complete eradication of primary treated tumors and distant untreated tumors in some mice implanted with the MB49 bladder cancer cells. The complete abscopal immune responses triggered further research interest in the characterization of the immunological mechanism of SYMPHONY. Hence, the dorsal skinfold window chamber mouse model as well as intravital microscopy of immune function were utilized in this thesis work.

1.5 Dorsal Skinfold Window Chamber Mouse Model

Window chamber techniques have the advantage of providing direct real-time access for high-resolution microscopy, while also ensuring longitudinal observation. In 1928, a rabbit ear chamber was implanted by J. C. Sandison to observe the blood vessel growth [20]. Later in 1939, the technique was adapted to observe angiogenesis and its influence on tumor growth by Ide and Warren [21]. Then the window chamber model was further developed, including the dorsal window chamber model, which is widely used in tumor xenograft and allograft animal studies today [22]. Palmer et al. described a specific surgery and imaging procedure using window chamber models (mammary or dorsal skinfold) to do high-resolution in vivo imaging of fluorescent proteins [23]. Chuan-Yuan Li et al. speculated the initial stage of tumor-cell-induced angiogenesis by transfecting the R3230Ac and 4T1 cell lines with a plasmid that constitutively expresses

enhance green fluorescence protein (EGFP) [24]. Sebstiaan et al. used dorsal window chambers for fluorescence localization and kinetics of meta-Tetrahydroxyphenylchlomin (mTHPC) [25]. Sobolik et al. used a mammary window chamber to evaluate leukocyte infiltration and cancer cell dissemination in mouse mammary tumors [31]. Benbenishty et al. planted a cranial window for intravital imaging which showed that CpG-C-activated microglia cells contact, kill, and phagocytize tumor cells in the early stages of tumor brain invasion more than nonactivated microglia [32].

The window chamber model also has its limitations. Like all the other surgical techniques, the surgical procedure could itself introduce an inflammatory response, which may complicate immunology studies. Additionally, compared to the orthotopic tumor microenvironment, the orthotopic stromal cells are not present.

1.6 Fluorescence Imaging and Intravital Microscopy of Immune Function

Dyes and stains have long been used to detect and visualize structures and processes in biological samples. Today, many of the favored dyes and stains have a fluorescent component because fluorescent molecules can be detected with extraordinary sensitivity and specificity.

"Fluorescence" is defined as the following process: some molecules are excited by absorbing light energy carried by photons to a higher energy state called an excited state, which is not stable for long. The unstable energy of the excited state is released

resulting in the emission of the light energy, and the molecules go back to the ground state. A molecule that is capable of fluorescing is so called a fluorophore. The emitted light, if it originates from endogenous chromophores, is called autofluorescence [1].

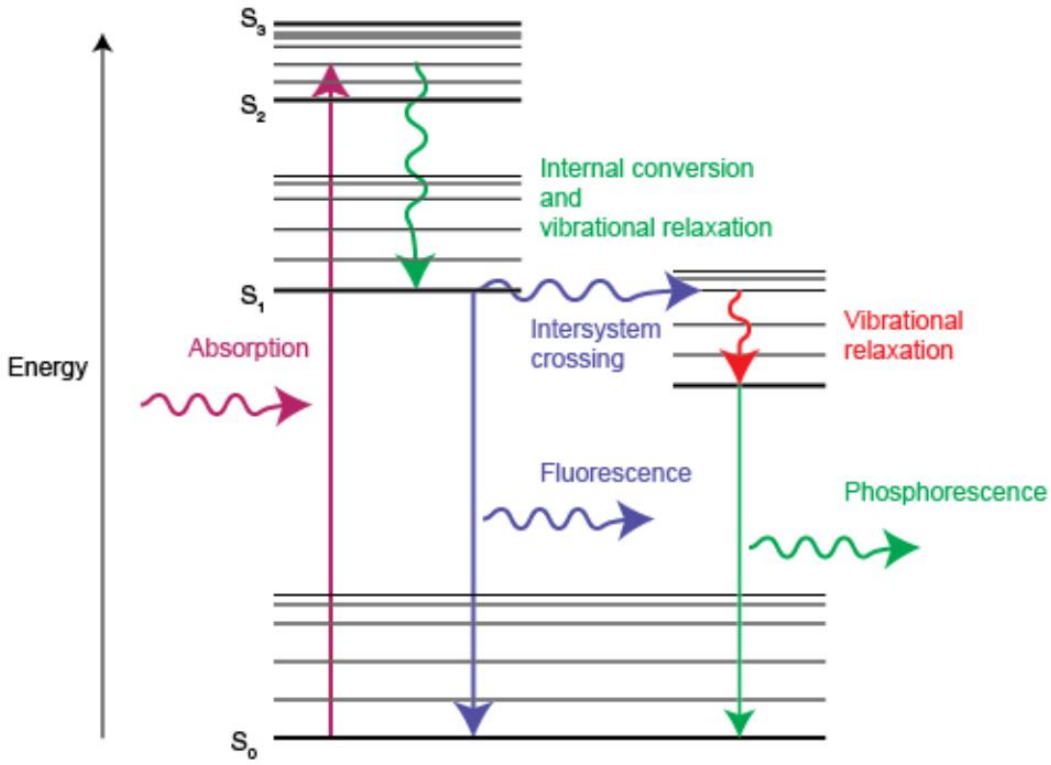

Figure 4: Energy diagram describing the process of fluorescence and phosphorescence [29]. When a molecule is excited to a high-energy state through the absorption of photons, it can decay back into its ground energy state through fluorescence (shown in blue) or phosphorescence (in green).

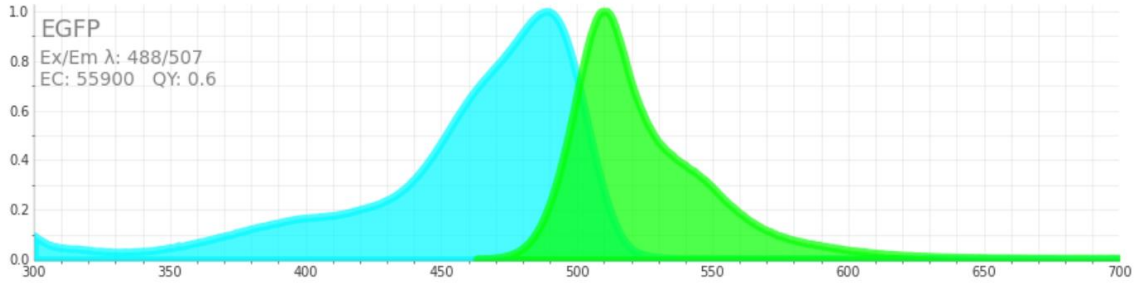

Figure 5: A typical absorption (in blue)/emission (in green) spectra of Enhanced Green Fluorescence Protein (EGFP) with excitation wavelength at 488 nm and emission wavelength at 507 nm [30]. EC: Extinction Coefficient (units: cm^{-1} M^{-1}) is defined as the c capacity for light absorption at a specific wavelength by the Beer-Lambert law A=EC•c•l, where A = absorbance, c = molar concentration, l = optical pathlength. QY: Quantum Yield is the number of fluorescence photons emitted per excitation photon absorbed. Fluorescence output per fluorophore ("brightness") is proportional to the product of the extinction coefficient (at the relevant excitation wavelength) and the fluorescence quantum yield.

The most used platform, wide field epi-fluorescence imaging, has simple settings, flexible temporal resolution (real-time imaging, time-lapse imaging available), good spatial resolution (typically 100nm – 1 mm, at the organelle to cell level), and straightforward data analysis. Appropriate filters are used to select the desired excitation wavelengths from a broad spectrum of light sources including lasers and LEDs. The ensuing fluorescence triggered by the light source is captured with a charge-coupled device (CCD) camera, the signal is recorded temporally on a computer and displayed on a monitor in near real-time.

Two types of images, reflectance (epifluorescence) and transmission, are commonly available on conventional fluorescence microscopes. Reflectance (epifluorescence) image is obtained when a dichroic beamsplitter is used to reflect the

excitation light to the sample and simultaneously transmit only the emitted light from the sample back to the detector placed on the same side. The transmission signal is captured by a detector placed on the opposite side of the excitation source. Most of the commercially available fluorescence microscopes utilize the epifluorescence mode because of its simplicity and to overcome problems with attenuation of light in thick samples [1].

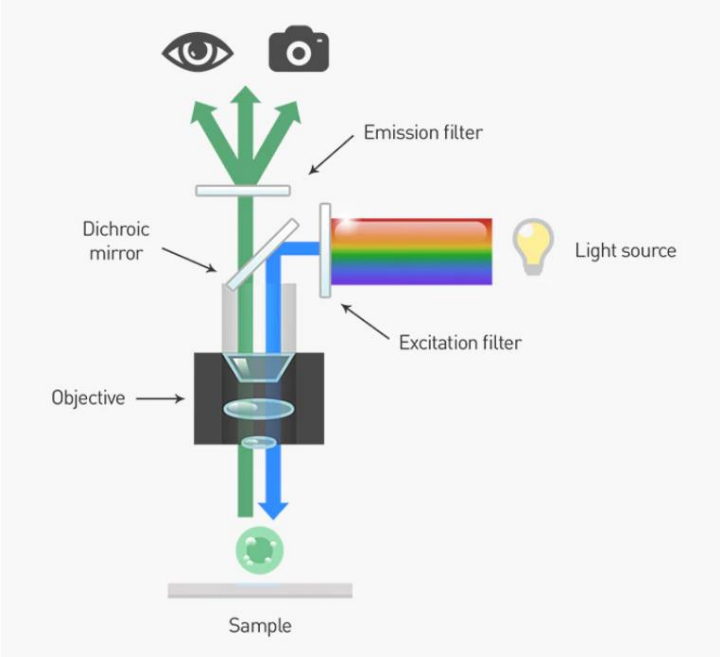

Figure 6: Typical light path in an epifluorescence microscope. Note that the both excitation and emission are controlled by the dichroic beamsplitter, which reflects excitation light (shorter wavelengths) onto the sample and passes the resulting emission light (longer wavelengths) through the emission filter and on to the detector (the viewer or the camera) [26].

For signal collection and analysis, the intensity of the emitted light and transmitted light are recorded in every pixel in the field of view, showing the location of

the chromophores. However, those planar images lose depth information, causing quantitative inaccuracy. The scattering of the emitted light also contributes to poor spatial resolution. To improve spatial resolution, especially in depth, a structured illumination technique is utilized, whose principle is similar to that of confocal imaging systems. Depth-sectioning is introduced to reconstruct a 3-D image although very thin in depth.

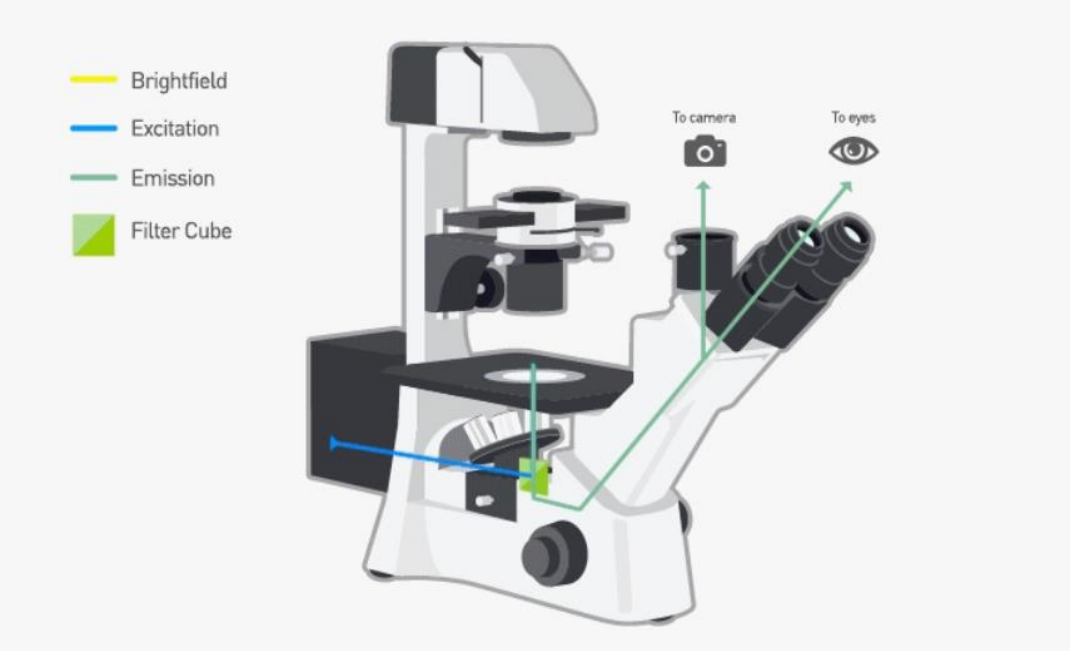

Figure 7: A diagram of a traditional epifluorescence microscope [26]. Here the blue line illustrates the path of excitation light, which travels through the filter cube and objective to the sample. The green line represents the light path of the resultant emission light which simultaneously travels through the objective and filter cube and onto the detectors. In epifluorescence microscopy, both the excitation and emission light travel through the same objective.

Owing to intravital microscopy's ability to quantitatively assess a wide variety of specific physiologic, molecular, and cellular targets at high resolution, the technique is particularly suitable for characterizing in vivo immune responses and tumor interactions. Fluorescence intravital microscopy, as one of the most commonly utilized subfields, has the advantage that within the same sample, multiple fluorophores can be used simultaneously due to different characteristic absorption and emission spectrum separation. Combined with genetic reporter methods, immunological studies could be widely developed. For example, in the CX3CR1-GFP model [31], which replaces the CX3CR1 gene with a green fluorescent reporter in the C57BL/6 background strain, immune cells are GFP-labeled, in particular monocytes, microglial cells, macrophages, and some NK and dendritic cells. In this study, mimicked-tumor-metastasis and immune cells were specifically labeled by red and green fluorescence, respectively, within the mice for detecting tumor location and immune intensity of the tumor location.

2. Materials and Methods

2.1 Apparatus and software

2.1.1 Apparatus

2.1.1.1 In vivo imaging system (IVIS): Zeiss Axio Observer Z.1 (Carl Zeiss Microscopy LLC, Thornwood, NY)

In this study, the advanced inverted epifluorescence microscope was used for window chamber images and calibration images acquisition. More details could be referred to 2.3. Image Acquisition.

2.1.1.2 Gas Anesthesia System: XGI-8 (Perkin Elmer Inc., Waltham, MA)

It delivers isoflurane gas to a 5-port anesthesia manifold housed in the IVIS imaging chamber. The manifold safely anesthetizes up to 5 adult mice simultaneously. The manifold also provides waste gas scavenging ports to help prevent gas from entering the surrounding work environment.

In this study, it was used for animal anesthesia for in vivo imaging. More details could be referred to 2.3. Image Acquisition.

2.1.2 Software

2.1.2.1 ZEN pro SP2012 (Carl Zeiss Microscopy LLC, Thornwood, NY)

ZEN pro SP2012 is a modular image-processing and analysis software for digital microscopy. In addition to basic functionality for image acquisition and microscope

definitions, elementary image processing and annotations, image analysis and documentation optional modules for specific tasks are available.

In this study, it was the operating software for image acquisition and exportation. More details could be referred to 2.4. Image Processing and Analysis.

2.1.2.2 ZEN Lite 3.0 Blue edition (Carl Zeiss Microscopy LLC, German)

ZEN Lite 3.0 Blue edition's functionalities include image acquisition, simple image processing, image analysis and documentation.

In this study, it was used for the shading correction.

2.1.2.3 ImageJ v1.52 (https://imagej.nih.gov/ij)

ImageJ is a public image processing software based on java, which is developed by the National Institutes of Health.

In this study, it was used for the stack focusing, tumor contour thresholding, ROI selection and measurements. More details could be referred to 2.4. Image Processing and Analysis.

2.2 Preparation of Mice before Imaging and Treatment Delivery

All procedures employed in this study were approved by the Duke University Institutional Animal Use and Care Committee.

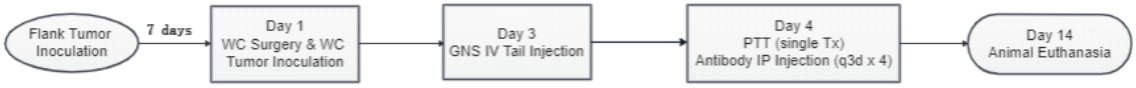

Figure 8: The flow of mice tumor inoculation and key treatment time points. Mice were imaged daily from Day 1 to Day 14. WC: window chamber; Antibody IP: Antibody intraperitoneal injection; q3d x 4: every 3 days for one dose of injection in total 4 times dose; PTT: photo thermal therapy.

2.2.1 Flank Tumor Cell Injections

250,000 MB49 bladder cancer cells per 100μL were implanted in the right flank of B6.129P2(Cg)-Cx3cr1tm1Litt/J Mice [31]. This mouse model was developed by replacing the CX3CR1 gene with an enhanced green fluorescent reporter in the C57BL/6 background strain. This strain of mice expresses EGFP in monocytes, dendritic cells, NK cells, and brain microglia under control of the endogenous Cx3cr1 locus. The hair on the right flank was removed 4 days before the flank tumor cell injection. These tumors took approximately 7-10 days to grow to a 100-150 mm^3 volume (right flank).

2.2.2 Dorsal Skinfold Window Chamber Surgeries and Dorsal Skinfold Tumor Cell Injections

The hair on the back of the mice was shaved 4 days before the dorsal window chamber surgeries. After 7 days from the flank inoculation, window chamber surgeries were performed (Day 1 for imaging), with 450,000 MB49 bladder cancer cells per 50μL injected into the center of the window chamber. On Day 3, mice were injected via the tail vein with Gold NanoStars (GNS) at a dose of 2mg in 100μL of PBS solution.

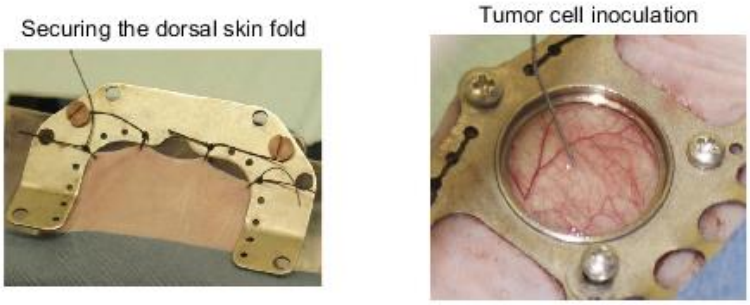

Figure 9: Dorsal window chamber surgery and tumor cell inoculation [23]. Note that the images cited here are from nude mice. However, the mice used in the SYMPHONY study are immune-competent, which necessitates the removal of their hair at dorsal skin and flank tumor inoculation sites.

2.2.3 Laser-induced Photothermal Therapy Delivery

One day after the GNS injection (Day 4), the laser-induced photothermal therapy was performed on the Laser group and SYMPHONY group mice (also note that it was performed after the injection of the antibody on Day 4). During the treatment, mice were anesthetized with 2% isoflurane and 1-2 L/min of oxygen delivered by the nose cone. An 808-nm laser (0.6 W/cm^2) was used to irradiate the right flank tumor 10 min in a single treatment. The laser operators wore laser safety goggles with OD 6 at 808 nm.

2.2.4 Anti-PD-L1 Immunotherapy Delivery

Mice of the anti-PD-L1 group and the SYMPHONY group were IP injected with 200μg anti-PD-L1 antibodies (10F.9G2 monoclonal antibody, Bio X Cell, NH) in 100μL PBS solution before the laser treatment on Days 4, 7, 10 and every 3 days until the end of

the experiment. Also, the imaging of the mice on that day was after the antibody injection.

2.2.5 Cells Labeling

In the WC study, MB49 bladder cancer cells were dyed with Vybrant DiD cell-labeling solution, which localizes cell membranes and lipids. This was done before inoculation into the WC. These cells could be detected by red fluorescence under the fluorescence microscope and flow cytometer.

For immune cells labeling, EGFP was expressed in monocytes, dendritic cells, NK cells, under control of the endogenous Cx3cr1 locus. They could be detected by green fluorescence under fluorescence microscopes and flow cytometers.

Table 1: Cells labeling.

Type	Labeling Method	Detection Method	For Use With (Equipment)
MB49 Bladder Cancer Cells	DiD Cell-labeling Solution Localized in Cell Membranes & Lipids	Red Fluorescent	Fluorescence Microscope, Flow Cytometer
CX3CR1 Locus Immune Cells	EGFP	Green Fluorescent	Fluorescence Microscope, Flow Cytometer

2.3 Image Acquisition

All image acquisition was done at Duke University School of Medicine Research Building 1 Room 289 on a Zeiss Axio Observer Z.1 Microscope. Its fluorescent lamp and cameras were turned on and warmed up for the recommended time, typically 5–20 min. A warming pad was also prepared to maintain the animal's body temperature during imaging under anesthesia. All images were acquired under 5X magnification.

2.3.1 Window Chamber Image Acquisition Procedure

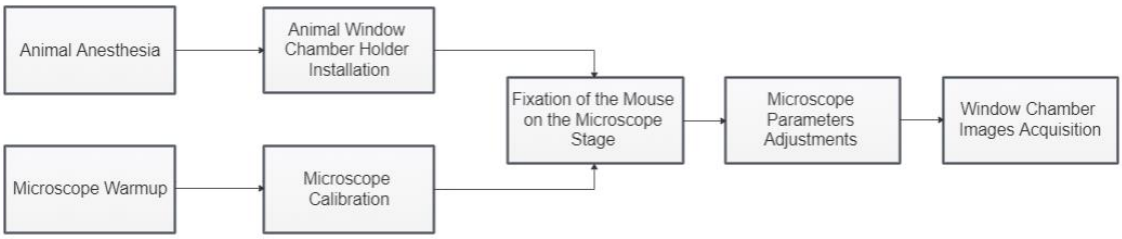

Figure 10: The flow of window chamber images acquisition. It could be simply divided into an animal-related part and a microscope-related part at first, and then combine the two parts together for later steps.

2.3.1.1 Animal Anesthesia

The Gas Anesthesia System,XGI-8 was set as the oxygen flow meter to 1-2 L/min and the isoflurane evaporation rate as 2% and connected to the anesthesia chamber. The mouse was put into the chamber for a 3-5 minutes' observation to confirm that it was fully anesthetized and its breathing rate was stable.

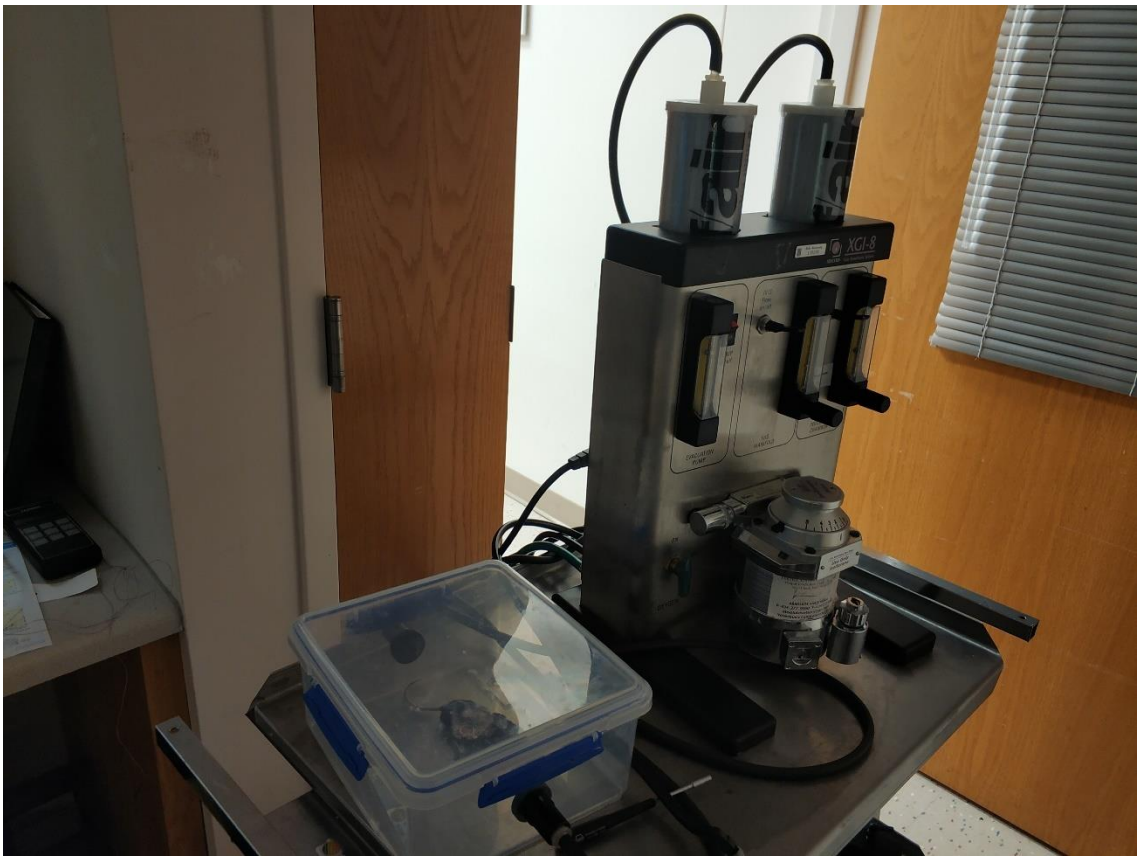

Figure 11: Animal anesthesia chamber and isoflurane vaporizer.

2.3.1.2 Window Chamber Holder Installation

After the mouse was anesthetized in the chamber, a transparent resin window chamber holder whose size is equal to a microscope slide was installed. It functioned as a holder to accurately fit into the black metal adapter of the microscope stage. The installation was operated in the anesthesia chamber.

2.3.1.3 Microscope Calibration

After the light source and the camera were warmed up, the ZEN pro SP2012 was opened and it was checked that the software was successfully connected with all components of the microscope. A calibration program of the software was run to calibrate the stage and focus of the microscope automatically. It took about 30 seconds.

2.3.1.4 Fixation of the Mouse on the Microscope Stage

The mouse was placed laterally with a warming pad in place that was set at 37℃. Its anesthesia status was maintained by nose cone connected to an isoflurane vaporizer. Eye lubricant was smeared on both eyes of the mouse for protection. The window chamber holder mentioned in 2.3.1.2 was fixed to the metal adapter on the stage horizontally.

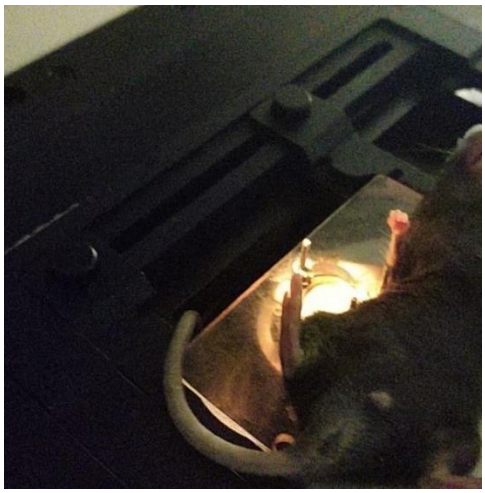

Figure 12: Fixation of the mouse on the microscope stage. A transparent resin window chamber holder whose size is equal to a microscope slide was installed.

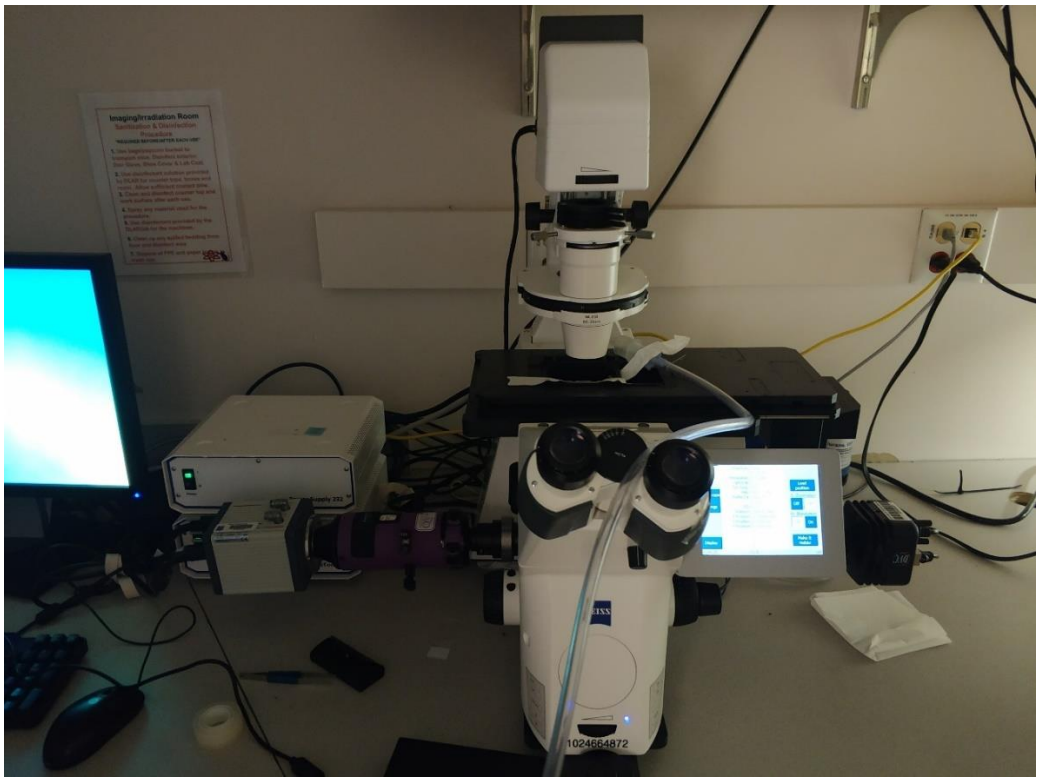

Figure 13: The Zeiss Axio Observer Z.1 Microscope. It has an operating panel on the right and its corresponding ZEN pro SP2012 software.

2.3.1.5 Microscope Parameters Adjustments

The center of the field was set for the tile imaging program. The optimal depth (Z-stack position) was selected where the capillaries were in the best focus under the brightfield channel. Two more z-positions were automatically set above and below the optimal depth respectively, with a 33 μm interval between each. The images of the total five z-positions were fused into one z-position later for conventional fluorescence analysis.

The optimal exposure times of each channel (brightfield, GFP, Cy5) were respectively set by adjusting the peak signal value to about half the saturation value. The reason for that was not only to avoid oversaturation but also to reduce photobleaching and phototoxicity. These settings were also checked to make sure that there was no saturation at the other sites.

After all the adjustments, the program was run to do tiled imaging, in which serial images were acquired in a grid pattern such that they could be stitched together to cover a wide field of view.

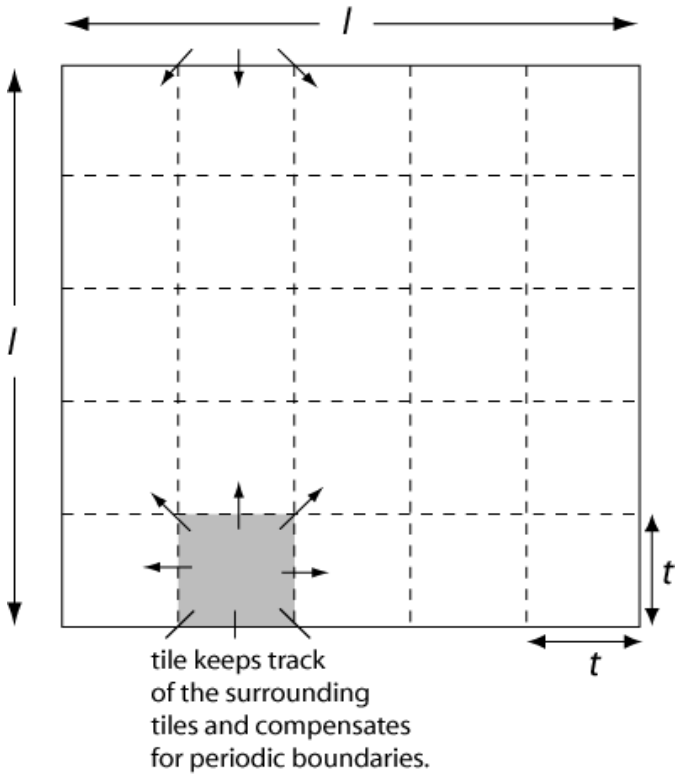

Figure 14: Plan view of a tiling example [36].

The figure below shows an example of the different image channels. The upper left one is the brightfield channel image showed in grayscale obtained by transitive light of a tungsten halogen light source. Since vessels have a high hemoglobin concentration, which has strong light absorption, they appear darker in the field of view (FOV). Also, the shadow area in the upper left of the window chamber is where the tumor cells were injected, and they can be seen to be forming a tumor at the location. The higher concentration of DiD (dye in the tumor cells) in the red fluorescence confirms the formation of a tumor in the bottom left image. From the upper right green fluorescence channel image, a higher intensity of GFP signal was recorded at the tumor area compared to the rest of the window chamber, indicating a greater number and higher density of immune cells in the tumor area. The fused three channels image in the bottom right could provide an overall illustration of the window chamber.

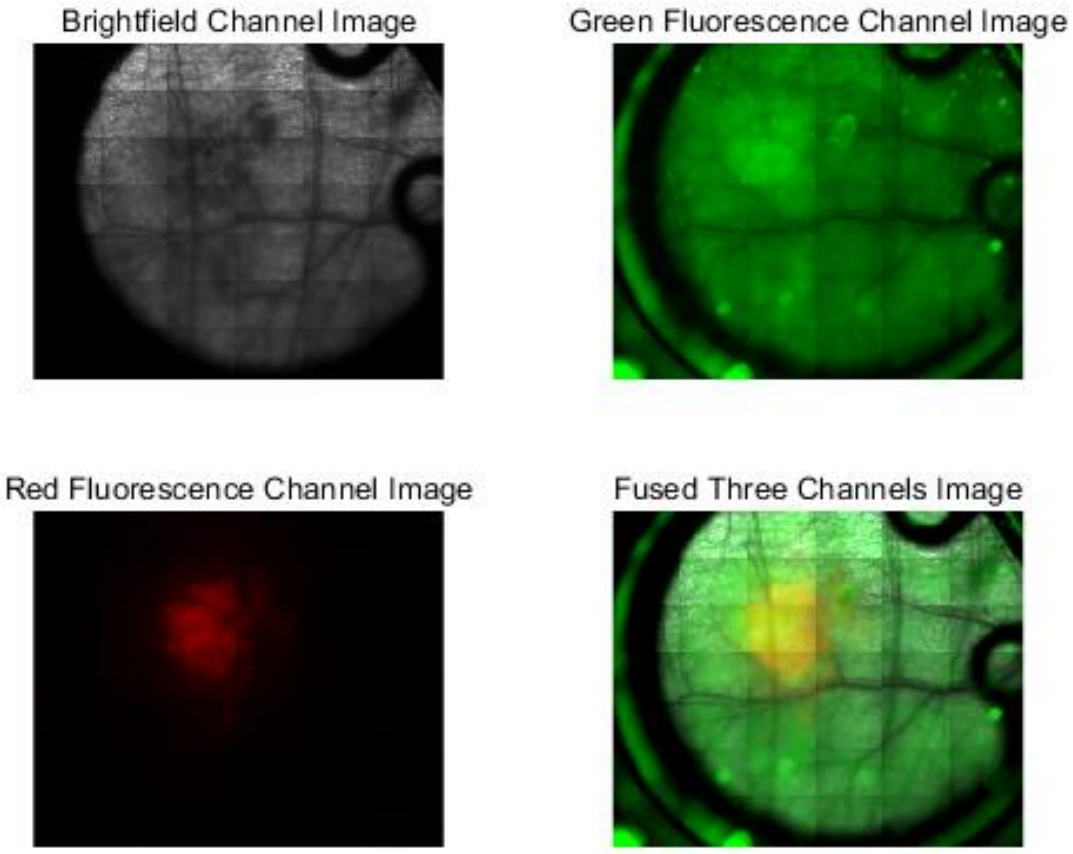

Figure 15: An illustration of the brightfield channel image, the green fluorescence channel image, the red fluorescence channel image and the fused three-channel image. The blood vessels can be clearly seen in the transmission brightfield channel. In the red fluorescence channel, tumor cells labeled with DiD show red fluorescence, which indicates the tumor location. In the green fluorescence channel, a higher intensity was recorded at the tumor location indicating a greater number of immune cells compared with the rest of the window chamber. The fused three channels image provides an overall illustration of the window chamber.

2.3.2 Calibration Images Acquisition

Calibration images were taken using calibration slides in which fluorophores are evenly distributed. In the perfect condition of the acquisition, the image of those calibration slides should also have a stable and consistent pixel value distribution. Since the illumination intensity and the system throughput in fact varies spatially, the information recorded in the calibration images can help in correcting the fluorescence pixel values for the window chamber. Calibration images of the GFP and CY5 channels were acquired daily.

In practice, the calibration images were acquired, by placing the calibration slide for each channel on the microscope and acquiring an image using the same settings as used during the experiment for that channel.

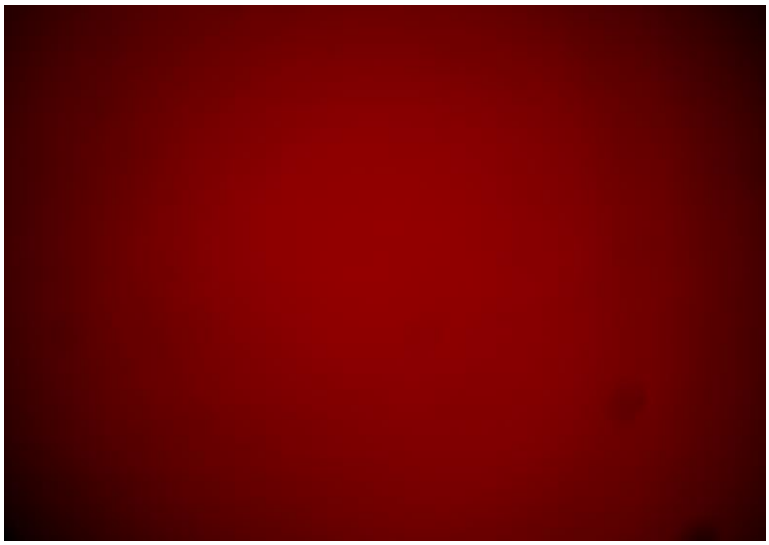

Figure 16: An example calibration image of CY5 channel. As can be seen from the figure, the intensity pattern is that signals were faded at four corners of the field of view, whereas thematically the intensity should be even across the image. Therefore, the calibration images provided us the correction baseline for the system throughput as a function of spatial location.

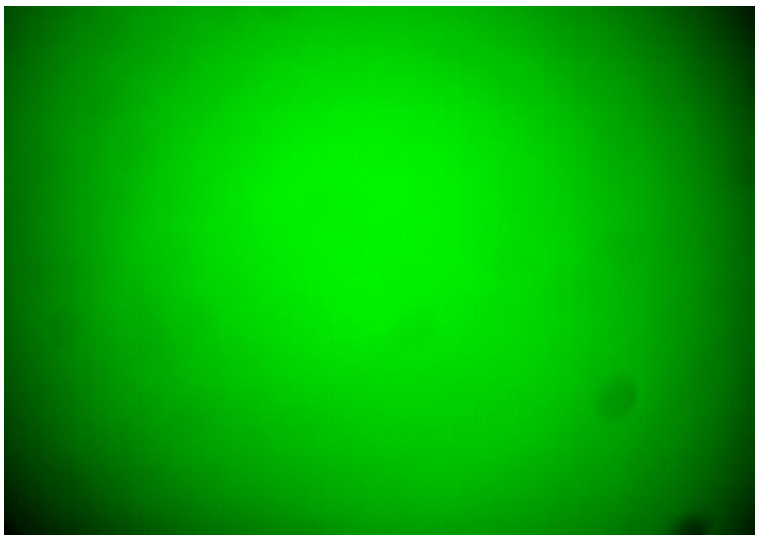

Figure 17: An example calibration image of GFP channel. A similar pattern can also be seen from the calibration image of the green fluorescence channel.

2.3.3 Dark Images Acquisition

Dark images are the electrical noise images created by the thermal noise of the camera's circuit. To record them, all the light paths were closed in ZEN and an image was acquired. Dark images were acquired daily.

The dark image is shown in the figure below, which demonstrates very low background signal.

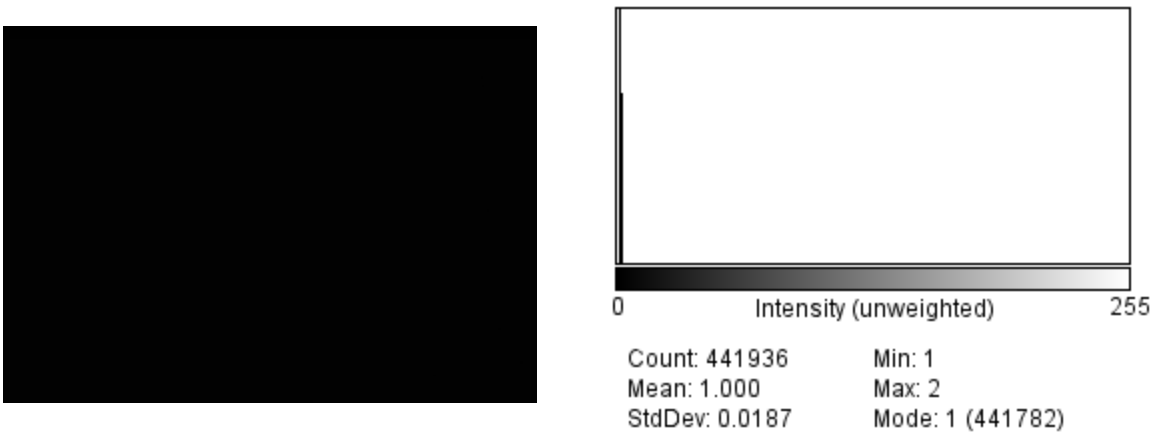

Figure 18: An example dark image and its histogram. The majority of the image is black. However, the spots of non-zero signals show the random distribution of the thermal noise, demonstrated in the histogram.

2.4 Image Processing and Analysis

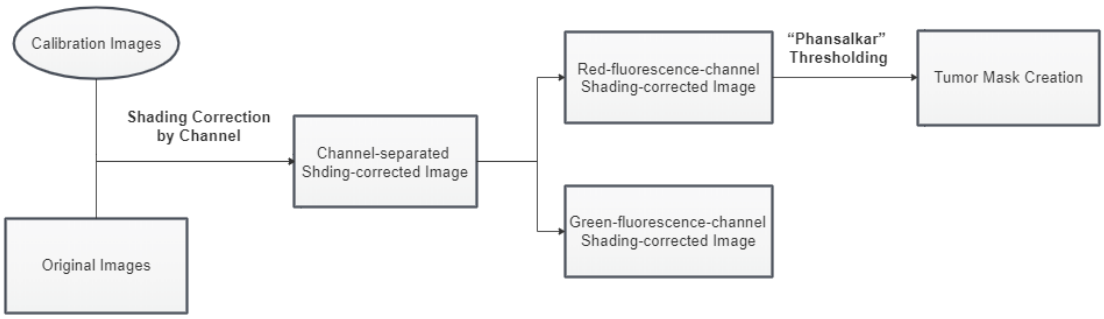

Figure 19: The flow of image processing.

2.4.1 Shading Correction

The process of shading correction can remove image structures that originate in the imaging system and do not belong to the actual image information. Without shading correction, the imaging system would cause image defects to be superimposed on the actual image information.

In this study, the shading correction was done by running the "shading correction" function on ZEN 3.0 Blue edition with the window chamber image as the input and the calibration image as the reference. GPF and Cy5 channel images were shading corrected with their corresponding calibration images, respectively.

2.4.2 Image Exportation

Since the original images were acquired and saved as czi files, which are the default file format of ZEN and the image analysis was on ImageJ, we exported the czi to

tiff files, channel by channel after shading correction, using ZEN's "export" function for further analysis in ImageJ. The dark images were also exported.

2.4.3 Fusion of Multi Z-position Images

The exported tiff files were separated by different Z-positions, which was not suitable for daily-based and channel-based image analysis. Therefore, a plugin of ImageJ called "stack focuser" was used to fuse the images from different Z-positions into one image for GFP and Cy5 channel, respectively. The fused images were displayed in conventional fluorescence mode, showing the integral fluorescence intensity of the tissue with 132 (33*4 intervals) μm thickness, although they do not achieve depth sectioning.

2.4.4 Tumor Contouring by Thresholding the Tumor Channel Fused Image

The tumor was contoured by creating a thresholded mask on the fused images of the Cy5 channel using the "Phansalkar" method [27] under "Auto Local Threshold" function of ImageJ. In this method, The local threshold T(x,y) is determined from the mean m(x,y) and standard deviation s(x,y) of the pixel intensities in a w pixel circular local window centered around the pixel (x, y) by the following equation:

$$T(x,y) = m(x,y)\left[1 + pe^{-q*m(x,y)} + k\left(\frac{s(x,y)}{R} - 1\right)\right]$$

where R is the dynamic range of standard deviation which is equal to 0.5 for a normalized image, k is a constant which takes values in the range [0.2,0.5], and p and q are constants (p = 2 and q = 10). Phansalkar recommends R = 0.5, k = 0.25.

The algorithm was initially designed for local thresholding for the detection of nuclei in diversity stained cytology images, but it was able to contour the edge of the tumor after we adjusted its parameters k and R.

After applying this step, the images were binarized. Then the "Analyze Particles" function was run under "Analyze" of ImageJ to record the location information of the tumor. The results were stored as a mask in the "ROI manager" in ImageJ.

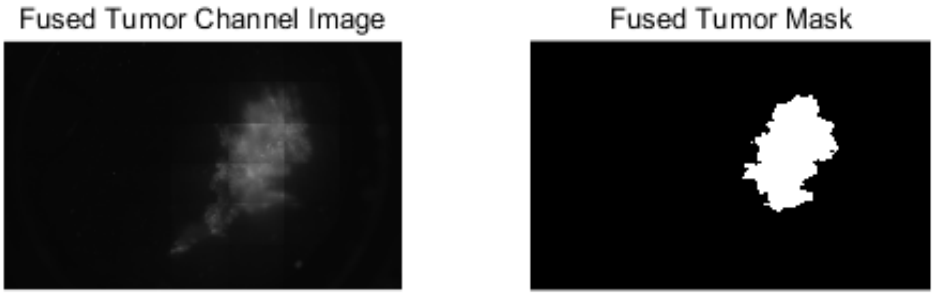

Figure 20: The fused tumor channel image (left) and the thresholded tumor mask (right). The mask is binarized from the original 16-bit fused image, and the tumor location information is recorded in the ROI manager.

2.4.5 Measurements of Pixel Value in the GFP Channel at Tumor Area and Non-tumor Area

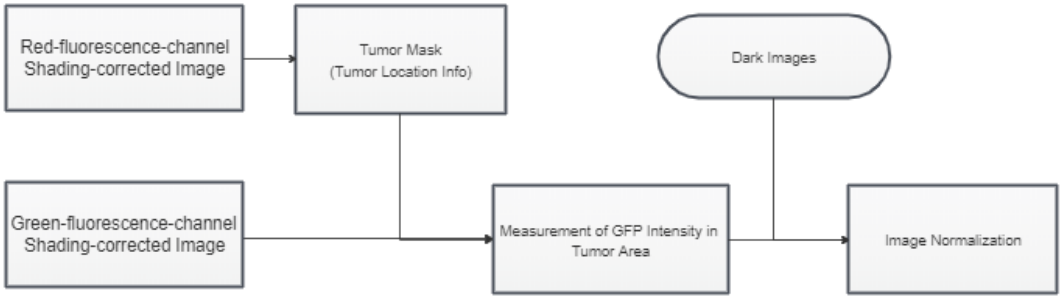

Figure 21: The flow of image analysis.

To measure the fluorescence intensity in the GFP channel in the tumor area, the fused tumor mask was applied to the fused GFP channel. The pixel value indicating the fluorescence intensity within the tumor area was measured using the "Analyze" function of ImageJ.

For the non-tumor area, ROIs were selected at places where it was relatively far from the tumor location but not close to the periphery of the window chamber and stayed consistent within each mouse.

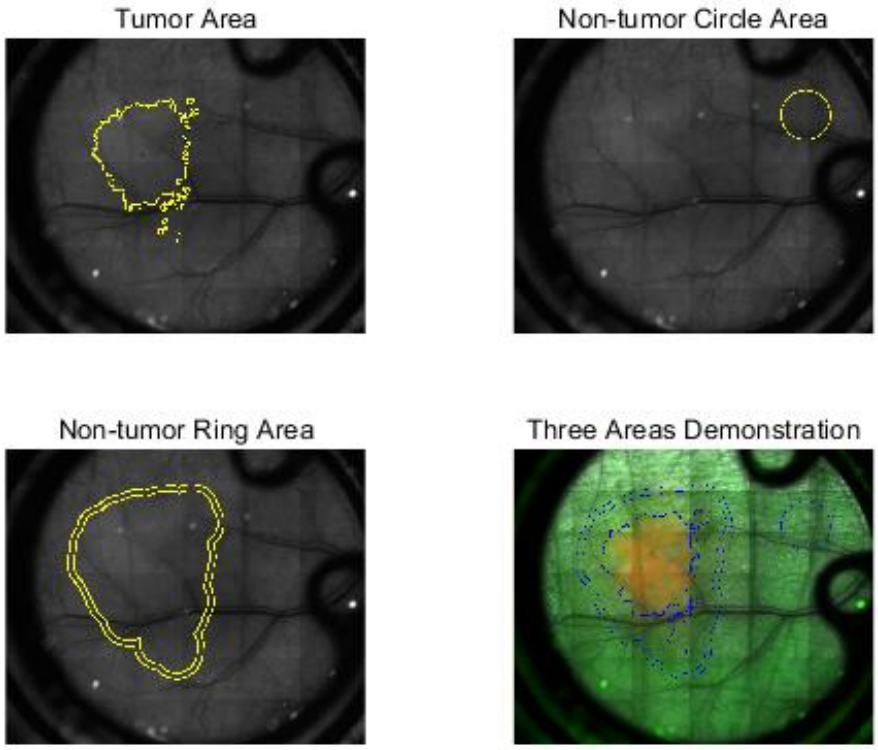

Figure 22: An illustration of the tumor area, the non-tumor circle area, the non-tumor ring area and the three areas demonstration. These three ROIs highlighted in yellow were applied on original raw data shown in grayscale in ImageJ. In the three areas demonstration, the same three ROIs were highlighted in blue and applied to the corresponding RGB image for better color contrast.

The mask of the tumor was applied on the fused GFP channel of the same day, as shown yellow-highlighted in the upper left figure.

The non-tumor circle area, as shown yellow-highlighted in the upper right figure, was identified at a region that was relatively far from the tumor but not close to the periphery of the window chamber to ensure it was distant from the tumor site while

avoiding noise and artifacts at the window edges. The radius of the circle was set 300 pixels (about 0.78 mm).

The non-tumor ring area was determined by enlarging the tumor contour edge by 230 pixels (about 0.60 mm) and then enlarging again by 70 pixels (about 0.18 mm), which means the width of the ring is 70 pixels (about 0.18 mm), spotted in the bottom left figure.

The three areas highlighted in blue in the bottom right shows that our contour of the tumor was in accordance with the fluorescence image.

2.4.6 Measurements of Pixel Value in Dark Images

The pixel values in the dark images indicating the thermal noise of the camera was measured using the "Analyze" function of ImageJ. Since the noise was consistent over the entire image, it was unnecessary to "mask" the dark images.

2.4.7 Signal Normalization

Since the images were acquired under different exposure times from day to day, which influences the pixel value, the measurements of the fluorescence intensity were normalized. The overall equation for normalization is (PV is for Pixel Value):

$PV_{normlized}$ = (PV of GFP mean – PV of Dark images)/Exposure Time

Then, the intensities were normalized to their pretreatment value (day 3's exposure time normalized value) to get the relative immune response ratio during the treatment.

To investigate the influence of the window chamber surgery before the treatment, the relative GFP intensity in the non-tumor area of the first 3 days was investigated with signal normalization to exposure time and then to their surgery day value (day 1's exposure time normalized value).

3. Results

In total 11 mice were imaged in 3 batches with specific information in the following table.

Table 2: Gender, experiment period and group information of the imaged mice. F: female; M: male.

Batch Name and Experiment Period	Batch E July 2019	Batch G September 2019	Batch H October 2019	Total number of each group
Number of Mice in SYMPHONY	1M	1M	2 (1F+1M)	4 (1F+3M)
Number of Mice in GNS + Laser	1F	1M	0	2 (1F+1M)
Number of Mice in GNS + anti-PD-L1	1M	1M	2 (1F+1M)	4 (1F+3M)
Number of mice in GNS only	0	0	1F	1F
Number of Mice in Total	3 (1F+2M)	3 (3M)	5 (3F+2M)	11 (4F+7M)

3.1 Four Groups Average Immune Intensity Comparison Over Time

Data points shown below are the mean immune intensity of each group after normalization to the exposure time only. Two-way ANOVA analysis concluded that there is no statistical significance between the groups.

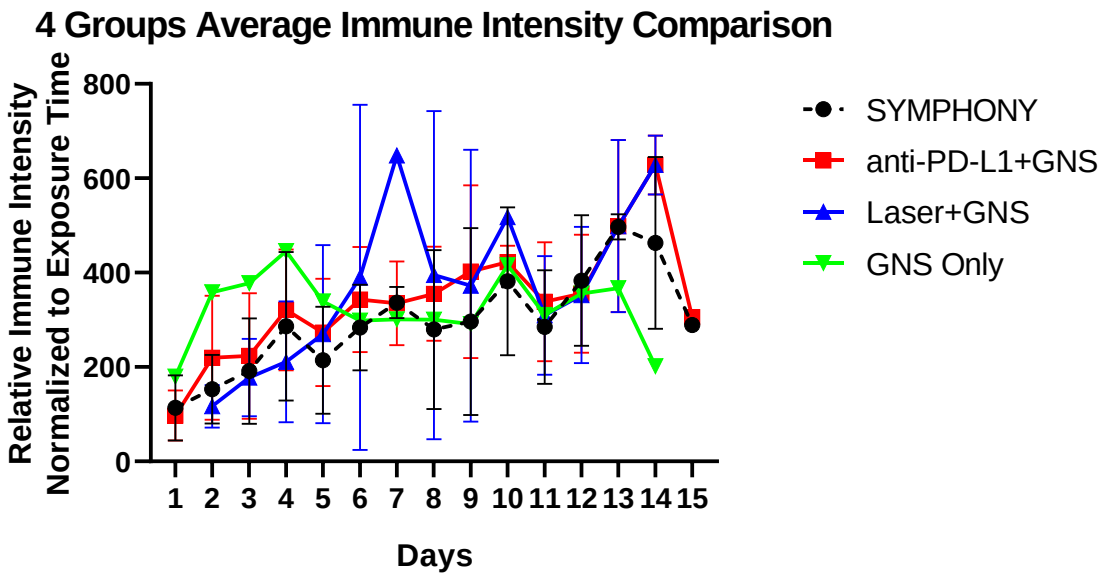

Figure 23: 4 groups average immune intensity comparison. The relative immune intensity was normalized to exposure time. Note that the GNS only group has only one mouse so far, which makes no error bars.

3.2 Four Groups Average Immune Intensity Ratio Comparison Over Time and Tukey's Multiple Comparisons between All Groups

Further, we normalized to pretreatment (Day 3) value to get the immune intensity ratio. Two-way ANOVA analysis still concluded that there is no statistical significance between the groups, time, or the combination of the two, which means no treatment method showed a statistically significant difference in immune response over other groups and no certain time point during the treatment was statistically significant.

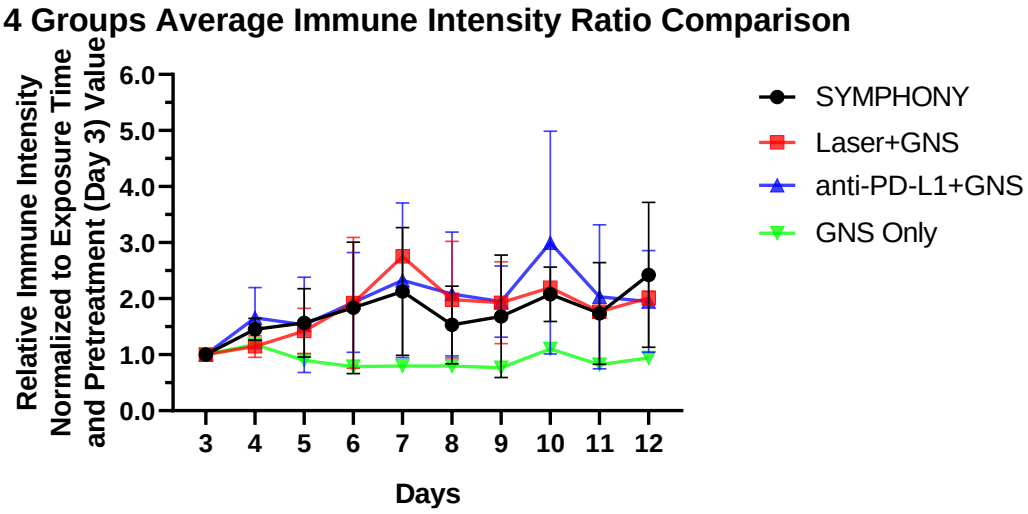

Figure 24: 4 groups average immune intensity ratio comparison. The relative immune intensity was normalized to exposure time and then normalized to pretreatment value (Day 3) to get the ratio.

For Tukey's multiple comparisons between all groups, statistical significance was found in anti-PD-L1+GNS vs GNS only, Laser+GNS vs GNS only, SYMPHONY vs GNS only, with p-values less than 0.0001, 0.002, and less than 0.001, respectively.

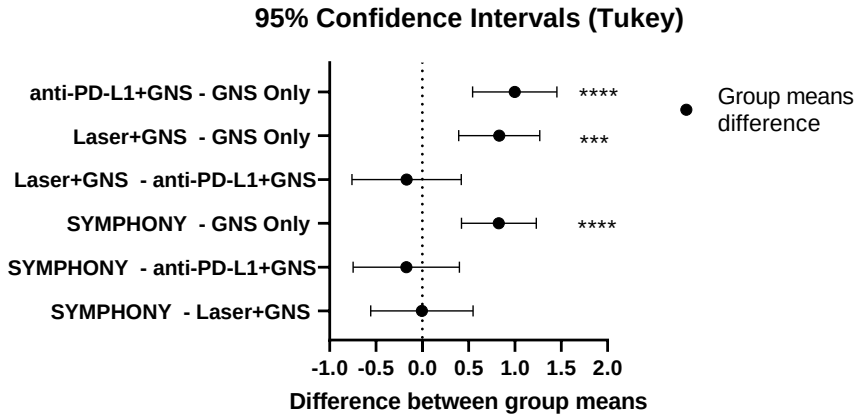

Figure 25: Tukey's multiple comparisons between each two groups. Statistical significance was found between every treatment group (anti-PD-L1+GNS, Laser+GNS,) vs the control group (GNS only).

3.3 Average Immune Intensity in Tumor Area VS Non-tumor Circle Area in Each Group

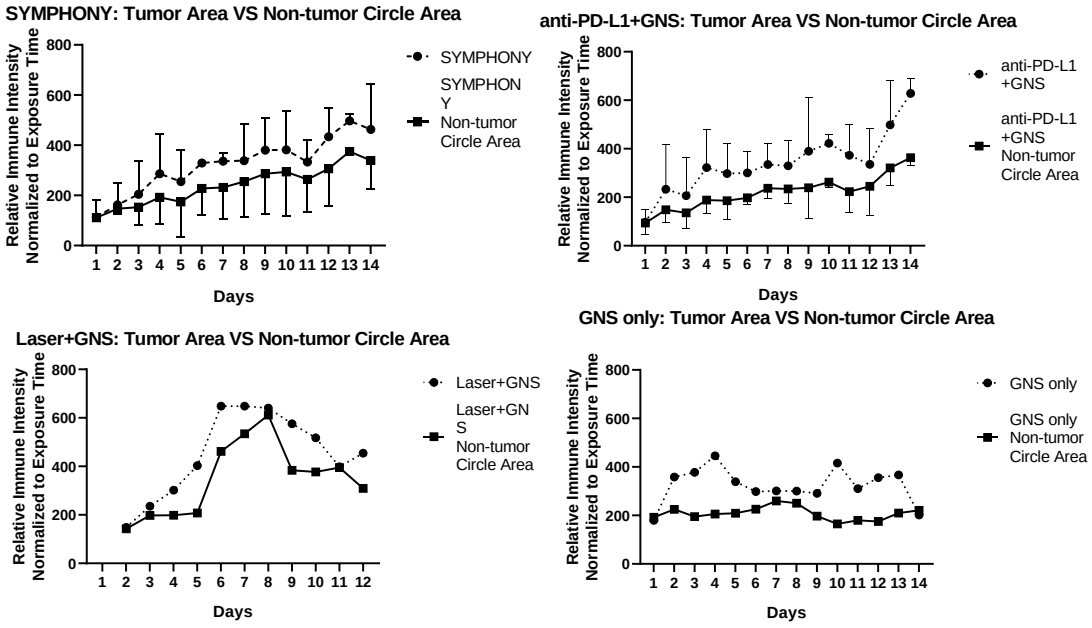

Figure 26: Tumor area vs non-tumor circle area in each group.

The comparison of relative immune intensity normalized to the exposure time between tumor area and non-tumor area in all groups indicates that the tumor area has a higher immune response. Statistical significance was observed in the treatment time factor using two-way ANOVA in the SYMPHONY and the anti-PD-L1+GNS group, whose p-value equals to 0.0248 and is less than 0.05, respectively.

3.4 Average Immune Intensity Ratio of Tumor Area to Non-tumor Circle Area in Each Group

Further, we got the average immune intensity ratio of the tumor area to the non-tumor circle area in each group. No statistical significance was found using two-way ANOVA.

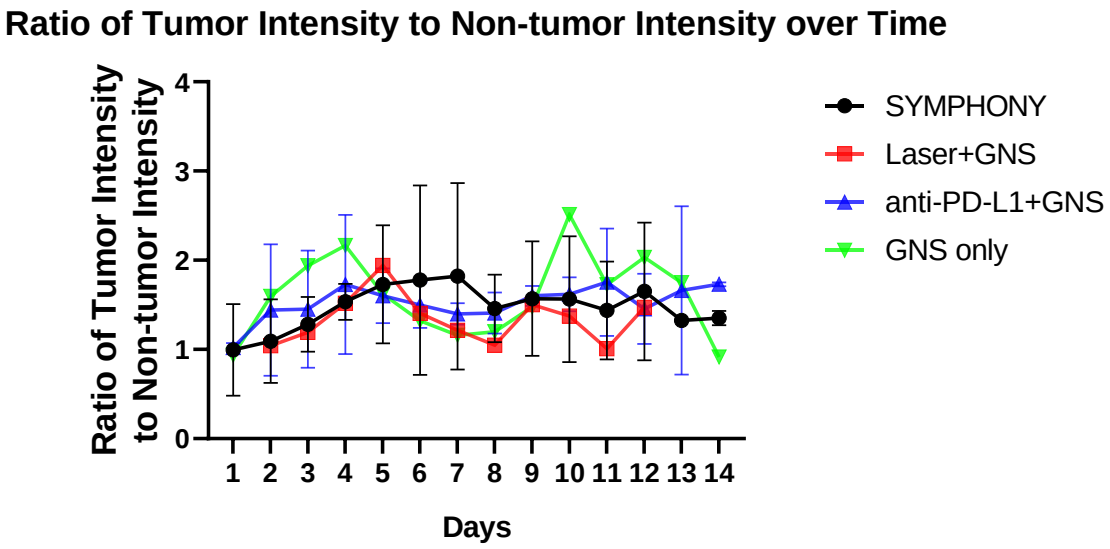

Figure 27: Average immune intensity ratio of the tumor area to the non-tumor circle area in each group.

3.5 Investigation of the Influence of the Window Chamber Surgery before the Treatment

An initial investigation of the influence of the window chamber surgery before the treatment was conducted on 5 mice's data at the non-tumor area and tumor area. Statistical significance was observed in both areas, with $p = 0.0313$ for the non-tumor area and $p = 0.0001$ for the tumor area.

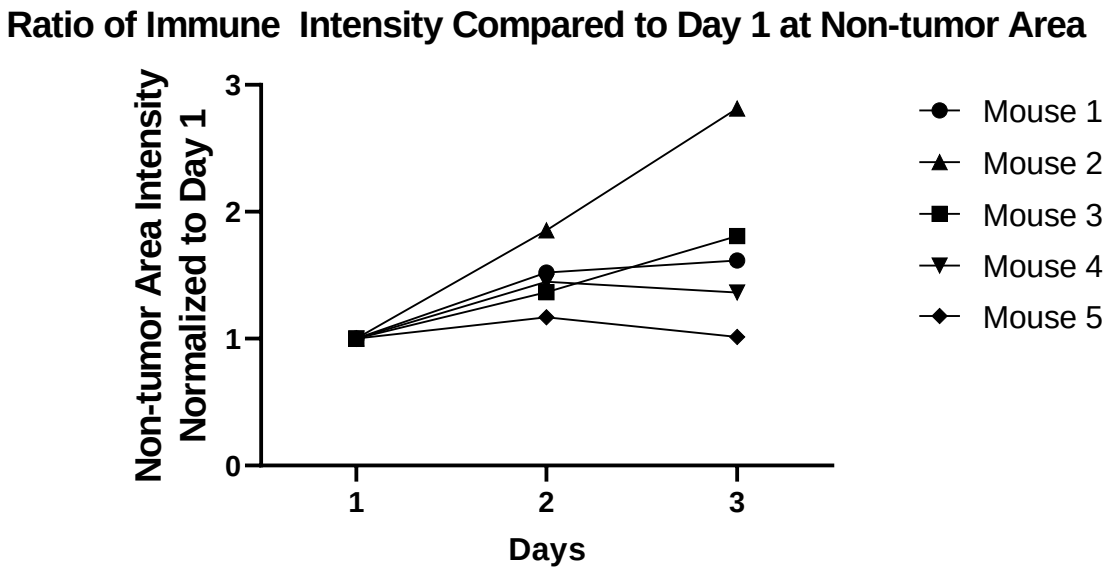

Figure 28: Ratio of Immune Intensity Compared to Day 1 at Non-tumor Area.

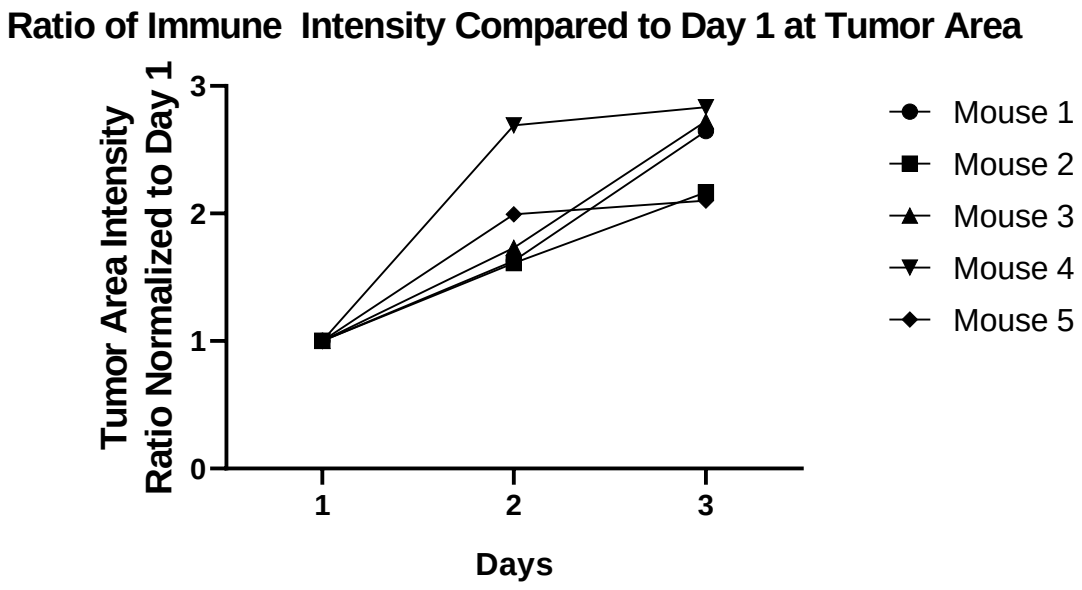

Figure 29: Ratio of Immune Intensity Compared to Day 1 at Tumor Area.

4. Discussion

Quantification of immune response following synergistic immune photothermal therapy (SYMPHONY) using optical imaging was demonstrated and proved to be feasible in this study. Higher fluorescence intensity from GFP generated by immune cells in the tumor region is significantly higher in all treatment groups than that of the non-tumor area. All three treatment groups have a higher immune response ratio than the control group. However, we did not observe that different treatment modalities (PTT only, GNS-PTT, IT, SYMPHONY) triggered different levels of the immune response. All treatment groups demonstrated similar immune responses, which is not in accordance with our hypothesis. Potential explanations for this are provided below.

4.1 Mouse Window Chamber Model

Since the window chamber surgery itself would trigger an immune response, which might deviate the normal immune environment around the original dorsal skin area of the mice, imaging the mice right after installing the window chambers is necessary to establish the baseline immune response level and evaluate the inflammatory response following the surgery.

After an initial investigation of the influence of the window chamber surgery before the treatment, the results showed that both areas had immune responses. The statistical significance of the tumor area was higher than of the non-tumor area.

The GNS was injected intravenously on Day 3 and the PTT would be performed on the next day, which allowed the circulation of GNS.

The image quality of the most window chamber images deteriorated as the time goes, with denser noise distribution, especially at the periphery of the field. The causes of this noise might be the stress of the coverslip of the window, inflammation, the deposition of collagen and autofluorescence.

4.2 Limitations

Since this study is only part of the SYMPHONY project, one limitation lies in the relatively small sample size. For the mouse strain we used, CX3CR1-GFP, the ideal sample size would be 44: 2 immunotherapy groups (anti-PD-L1, control) x 2 PTT groups (GNS PTT, control) x 10 animals per group (5 male and 5 female), adjusted for 10% dropout/loss. Therefore, more mice could be added to fill the gap between the current treatment groups and control groups.

One of the major purposes of this study is to assess the abscopal effect in vivo through the window chamber technique. The tumor cells injected into the window chamber mimic distant metastases while the flank tumor injection serves as the primary tumor that received treatment. However, further assessments could be applied on whether the tumor cells injected into the window chamber grow into a solid tumor, and how its microenvironment is close to that of tumor metastasis. From the tumor channel

images we observed, some of the tumor dye fluorescence distribution showed limited expansion in the field of view compared to the baseline pattern. This might indicate that there are tumor suppressive factors like antiangiogenic factors produce in the primary tumor that could affect the secondary tumor, which has been reported for a variety of tumors. It may also be an effect of the treatment.

One of the major factors that contribute to the image quality deterioration of the window chamber in this study is the skin hair regrowth. In the later period of the imaging follow-up, the regenerated hair from the shaved site made the tissue under the window chamber thicker and more heterogeneous. This phenomenon is unavoidable since we could not use the immune-deficient nude mice for this study as we required immune component animals. Therefore, if we could introduce a correction factor for hair regeneration, it would further improve the accuracy of fluorescence measurements. One assumption would be to have some mice that only installed window chambers but without treatments. They would be imaged under the same procedure and microscopic settings so that the hair regeneration would be the only factor that may contribute to the intensity changes. After averaging the hair regeneration-lead intensity changing ratio from these blank mice, a correction factor for hair regeneration can be obtained.

4.3 Future Work

Flow cytometry experiments are being planned to clarify which immune cell subtypes are represented by the GFP+ cells within the tumor, from the tumor and immune organs we collected after the mice euthanasia. It allows the detection and quantitation of individual fluorescent cells within a population since the flow cytometer measures and analyzes the optical properties of hundreds of single cells per second passing through a focused laser beam. Chu et al. (1999) used the murine myeloid leukemic cell line transfected with a GFP-encoding plasmid. Following fixation in different formaldehyde concentrations and permeabilization with 70% ethanol, cells were stained with PI and analyzed by flow cytometry for GFP fluorescence and DNA content [28].

More mice would be added to fit the ideal sample size and a more complete data analysis would be conducted. A correction factor for resolving the image quality deterioration is under research. Further assessment of the cell-killing effect can be conduction in analyzing the tumor activity change of the normalized tumor signal in the window chamber.

Also, higher resolution imaging at single-cell level would contribute to further investigating the immune response. Other imaging modalities like MR or ultrasound

could also be introduced in assisting the detection of window chamber tumor growth and the correction of hair regrowth.

5. Conclusions

Synergistic immune photothermal therapy (SYMPHONY) is the combination of nanoparticle-mediated photothermal therapy and immune checkpoint inhibitor immunotherapy. Four groups of B6.129P2(Cg)-*Cx3cr1*^{tm1Litt}/J Mice were optically imaged using the window chamber model to study the primary and abscopal immune response. According to the data collected so far, no significance was shown among the groups in the immune intensity within the window chamber. Higher responses were observed in the tumor areas compared to the non-tumor areas. The initial investigation of the effect of the window chamber surgery showed no significant immune response was triggered in normal tissue. The fluorescence imaging along with the window chamber technique demonstrates the feasibility and convenience following such a longitudinal study like SYMPHONY.

References

[1] Metasebya, S. , Yang, L. , Berezin, M. Y. , & Samuel, A. . (2011). Optical imaging in cancer research: basic principles, tumor detection, and therapeutic monitoring. *Medical Principles & Practice International Journal of the Kuwait University Health Science Centre*, *20*(5), 397-415.

[2] Falk, M. H. , & Issels, R. D. . (2001). Hyperthermia in oncology. *International Journal of Hyperthermia*, 17(1), 1-18.

[3] Hildebrandt, B. , Wust, P. , Ahlers, O. , Dieing, A. , Sreenivasa, G. , & Kerner, T. , et al. (2002). The cellular and molecular basis of hyperthermia. *CRITICAL REVIEWS IN ONCOLOGY HEMETOLOGY*.

[4] Frey, B. , Weiss, E. M. , Rubner, Y. , Wunderlich, R. , & Gaipl, U. S. . (2012). Old and new facts about hyperthermia-induced modulations of the immune system. *International Journal of Hyperthermia*, 28(6), 528-542.

[5] Schildkopf, P., J Ott, O., Frey, B., Wadepohl, M., Sauer, R., Fietkau, R., & S Gaipl, U. (2010). Biological rationales and clinical applications of temperature controlled hyperthermia-implications for multimodal cancer treatments. *Current medicinal chemistry*, *17*(27), 3045-3057..

[6] Maeda, Hiroshi, Tsukigawa, Kenji, & Fang, Jun. . A retrospective 30?years after discovery of the enhanced permeability and retention effect of solid tumors: next-generation chemotherapeutics and photodynamic therapy-problems, solutions, and prospects. *Microcirculation*, 23(3), 173-182.

[7] Yuan, H., Khoury, C. G., Hwang, H., Wilson, C. M., Grant, G. A., & Vo-Dinh, T. (2012). Gold nanostars: surfactant-free synthesis, 3D modelling, and two-photon photoluminescence imaging. *Nanotechnology*, *23*(7), 075102.

[8] Liu, Y., Ashton, J. R., Moding, E. J., Yuan, H., Register, J. K., Fales, A. M., ... & Ma, Y. (2015). A plasmonic gold nanostar theranostic probe for in vivo tumor imaging and photothermal therapy. *Theranostics*, *5*(9), 946.

[9] Moy, A. J., & Tunnell, J. W. (2017). Combinatorial immunotherapy and nanoparticle mediated hyperthermia. *Advanced drug delivery reviews*, *114*, 175-183.

[10] Siegel, R. L., Miller, K. D., & Jemal, A. (2016). Cancer statistics, 2016. *CA: a cancer journal for clinicians*, *66*(1), 7-30.

[11] Botteman, M. F. , Pashos, C. L. , Redaelli, A. , Laskin, B. , & Hauser, R. . (2003). The health economics of bladder cancer: a comprehensive review of the published literature. *PharmacoEconomics, 21*(18), 1315-1330.

[12] Siegel, R., DeSantis, C., Virgo, K., Stein, K., Mariotto, A., Smith, T., ... & Lin, C. (2012). Cancer treatment and survivorship statistics, 2012. *CA: a cancer journal for clinicians*, *62*(4), 220-241.

[13] Stenzl, A., Cowan, N. C., De Santis, M., Kuczyk, M. A., Merseburger, A. S., Ribal, M. J., ... & Witjes, J. A. (2011). Treatment of muscle-invasive and metastatic bladder cancer: update of the EAU guidelines. *European urology*, *59*(6), 1009-1018.

[14] Alexandroff, A. B., Jackson, A. M., O'Donnell, M. A., & James, K. (1999). BCG immunotherapy of bladder cancer: 20 years on. *The Lancet*, *353*(9165), 1689-1694.

[15] Herr, H. W., & Morales, A. (2008). History of bacillus Calmette-Guerin and bladder cancer: an immunotherapy success story. *The Journal of urology*, *179*(1), 53-56.

[16] Inman, B. A., Sebo, T. J., Frigola, X., Dong, H., Bergstralh, E. J., Frank, I., ... & Kwon, E. D. (2007). PD-L1 (B7-H1) expression by urothelial carcinoma of the bladder and BCG-induced granulomata: associations with localized stage progression. *Cancer: Interdisciplinary International Journal of the American Cancer Society*, *109*(8), 1499-1505.

[17] Dong, H., Strome, S. E., Salomao, D. R., Tamura, H., Hirano, F., Flies, D. B., ... & Lennon, V. A. (2002). Tumor-associated B7-H1 promotes T-cell apoptosis: a potential mechanism of immune evasion. *Nature medicine*, *8*(8), 793-800.

[18] Frigola, X., Inman, B. A., Krco, C. J., Liu, X., Harrington, S. M., Bulur, P. A., ... & Kwon, E. D. (2012). Soluble B7-H1: differences in production between dendritic cells and T cells. *Immunology letters*, *142*(1-2), 78-82.

[19] Garg, A. D., Nowis, D., Golab, J., Vandenabeele, P., Krysko, D. V., & Agostinis, P. (2010). Immunogenic cell death, DAMPs and anticancer therapeutics: an emerging amalgamation. *Biochimica et Biophysica Acta (BBA)-Reviews on Cancer*, *1805*(1), 53-71.

[20] Sandison, J. C. (1928). Observations on the growth of blood vessels as seen in the transparent chamber introduced into the rabbit's ear. *American Journal of Anatomy*, *41*(3), 475-496.

[21] Ide, A. G. (1939). Vascularization of the Brown-Pearce rabbit epithelioma transplant as seen in the transparent ear chamber. *Am. J. Roentg.*, *42*, 891.22 oninvasive visualization of tumors in rodent dorsal skin window chamber

[23] Palmer, G. M., Fontanella, A. N., Shan, S., & Dewhirst, M. W. (2012). High-resolution in vivo imaging of fluorescent proteins using window chamber models. In *In Vivo Cellular Imaging Using Fluorescent Proteins* (pp. 31-50). Humana Press, Totowa, NJ.

[24] Li, C. Y., Shan, S., Huang, Q., Braun, R. D., Lanzen, J., Hu, K., ... & Dewhirst, M. W. (2000). Initial stages of tumor cell-induced angiogenesis: evaluation via skin window chambers in rodent models. *Journal of the National Cancer Institute*, *92*(2), 143-147.

[25] de Visscher, S. A., Kaščáková, S., de Bruijn, H. S., van den Heuvel, A. V. D. P., Amelink, A., Sterenborg, H. J., ... & Witjes, M. J. (2011). Fluorescence localization and kinetics of mTHPC and liposomal formulations of mTHPC in the window-chamber tumor model. *Lasers in surgery and medicine*, *43*(6), 528-536.

[26] Molecular probes school of fluorescence (2020, January 7). Epifluorescence microscope basics from https://www.thermofisher.com/cn/en/home/life-science/cell-analysis/cell-analysis-learning-center/molecular-probes-school-of-fluorescence/imaging-basics/fundamentals-of-fluorescence-microscopy/epifluorescence-microscope-basics.html

[27] Phansalkar, N. , More, S. , Sabale, A. , & Joshi, M. . (2011). Adaptive local thresholding for detection of nuclei in diversity stained cytology images. *International Conference on Communications & Signal Processing*. IEEE.

[28] Chu, Y. W., Wang, R., Schmid, I., & Sakamoto, K. M. (1999). Analysis with flow cytometry of green fluorescent protein expression in leukemic cells. *Cytometry: The Journal of the International Society for Analytical Cytology*, *36*(4), 333-339.

[29] Rickard, Ashlyn (2017). *The Development of an In Vivo Mobile Dynamic Microscopy System that Images the Hypoxic Microenvironments of Cancerous Tumors via Fluorescent and Phosphorescent Nanoparticles.* Master's thesis, Duke University. Retrieved from https://hdl.handle.net/10161/15270.

[30] FPbase for fluorescent proteins (FPs) and their properties (2020, May 15). EGFP from https://www.fpbase.org/protein/egfp/

[31] Sobolik, T. , Su, Y. J. , Ashby, W. , Schaffer, D. K. , Wells, S. , & Wikswo, J. P. , et al. (2016). Development of novel murine mammary imaging windows to examine wound healing effects on leukocyte trafficking in mammary tumors with intravital imaging. *IntraVital*.

[32] Benbenishty, A., Gadrich, M., Cottarelli, A., Lubart, A., Kain, D., Amer, M., Shaashua, L., Glasner, A., Erez, N., Agalliu, D., Mayo, L., Ben-Eliyahu, S., & Blinder, P. (2019). Prophylactic TLR9 stimulation reduces brain metastasis through microglia activation. *PLoS biology*, *17*(3), e2006859.

[33] Meng, X. , Huang, Z. , Teng, F. , Xing, L. , & Yu, J. . (2015). Predictive biomarkers in pd-1/pd-l1 checkpoint blockade immunotherapy. Cancer Treatment Reviews, 41(10), 868-876.

[34] Li, R. , Zheng, K. , Yuan, C. , Chen, Z. , & Huang, M. . (2017). Be active or not: the relative contribution of active and passive tumor targeting of nanomaterials. Nanotheranostics, 1(4), 346-357.

[35] Liu, Y., Maccarini, P., Palmer, G. M., Etienne, W., Zhao, Y., Lee, C. T., ... & Vo-Dinh, T. (2017). Synergistic immuno photothermal nanotherapy (SYMPHONY) for the treatment of unresectable and metastatic cancers. Scientific reports, 7(1), 1-6.

[36] Alberts, L. J. H. (2005). Initial porosity of random packing: computer simulation of grain rearrangement.